

Chapter 6

Development of Fabrication Processes for AlN Photonic Crystal Nanocavities

6.1 Introduction

Quantum cryptography in which quantum states are used to transport some key information with perfect security have been proposed and intensively studied. Since attenuated light sources emitting coherent photons with Poissonian statistics have limitations in practical implementation ^[122, 123], sources emitting triggered single-photons on demand are increasingly expected. At present, various candidates for the single-photon emitter such as atoms ^[28], ions ^[124], molecules ^[27], or imperfections in solids ^[125] have been demonstrated. Compared to them, epitaxially-grown semiconductor quantum dots have some attractive advantages: they can easily be integrated into compact, monolithic practical devices, into which carriers are injected by current ^[35]. However, conventional III-V quantum dots most commonly used as solid-state single-photon sources such as InAs quantum dots can inherently be operated only at around liquid-helium temperatures. III-nitride quantum dots have potentials to emit single photons at much higher temperatures owing to their material nature including large exciton binding energies. So far, we have demonstrated single-photon generation from GaN/AlN quantum dots up to 200 K ^[36]. A short-wavelength single-photon emitter is beneficial for free-space quantum telecommunication because diffraction loss can be reduced as wavelength is shortened. That also implies smaller volume of antennas is available, which is a great advantage for satellite-based quantum key distribution system.

Another issue concerning previously reported solid-state single-photon emitters using semiconductor quantum dots is their low efficiency. As already demonstrated, structures such as mesas or optical cavities have been employed to improve light extraction efficiency of single-photon

emitters ^[30, 126]. Quantum efficiency also can be improved through the control of photon density of states by utilizing three-dimensional cavities. Photonic crystal nanocavities with high quality factor (Q -factor) and small mode volume are capable of exhibiting strong Purcell enhancement and of modifying radiation pattern. Hence they can greatly improve the performance of single-photon emitters ^[40]. However, there are technological challenges in fabricating photonic crystals with III-nitride materials: small feature size is required corresponding their emission wavelength, microfabrication process is hard due to their material inertness, and requirement for air-bridge structure to achieve better optical confinement make the fabrication process far more difficult. Previous efforts concerning nitride-based photonic crystals have been mainly focused on improvement of light extraction efficiency of blue/violet light-emitting diodes ^[127, 128] and only a few reports have described PC nanocavity exhibiting cavity modes in blue/violet region ^[129]. Choi et al. fabricated GaN photonic crystal membrane nanocavities by selectively etching an InGaN sacrificial layer grown beneath the GaN layer. They obtained Q -factor of around 800, which was lower than theoretically expected ^[129]. Although InGaN quantum-dot structures can be embedded in GaN matrix ^[130, 131], single-photon generation from InGaN quantum dots has not been demonstrated yet.

In this chapter, the author report the first successful fabrication of air-bridge AlN photonic crystal nanocavity with GaN quantum dots. Developments of fabrication processes for the nanocavities are described in detail. Preliminary calculations reveal technological requirements for the fabrication. In addition to the requirement for fine patterns as small as 150-nm-period, the substrate must be removed in order to obtain sufficient optical confinement in the nanocavities. Photoelectrochemical etching techniques are employed to obtain AlN convex-shaped air-bridge structures. Energy band discontinuity at epitaxial layer/substrate interface and strain inside the epitaxial layer were utilized in our novel fabrication process. Due to accumulated photogenerated holes, lateral etching of 6H-SiC substrate occurs just below the AlN/SiC interface, and partial lift-off of AlN epitaxial layer results in a convex-shaped air-bridge structure.

6.2 Design of AlN photonic crystals

The concept of photonic crystal was first proposed by Yablonovitch ^[38] and John ^[132]. Electrons in solids can be described by wavefunctions and due to this nature there appears so-called energy bandgaps. Electrons are prohibited to have energies corresponding to within the gap. And Yablonovitch suggested that analogous phenomena can be realized with electromagnetic waves. By

facilitating periodically modulated dielectric structures, one can obtain photonic bandgap within which propagation of electromagnetic waves with frequencies corresponding to the gap are prohibited. Yablonovitch suggested that by utilizing photonic crystals, one can control spontaneous emission with frequencies within the photonic bandgap^[38].

On the other hand, from analogy between Schrödinger and Maxwell equations John suggested that fluctuations in periodic dielectric structure can localize electromagnetic waves^[132]. That is an analogy of Anderson localization in solid state physics.

From Maxwell equations, one can obtain

$$\left[-\nabla^2 + \nabla(\nabla \cdot) - \frac{\omega^2}{c^2} \varepsilon_{\text{fluc}}(r) \right] \mathbf{E}(\mathbf{r}) = \frac{\omega^2}{c^2} \mathbf{E}(\mathbf{r}). \quad (6.1)$$

In the above equation, c is the speed of light in vacuum, while ω and $\mathbf{E}(\mathbf{r})$ stand for the frequency and the electric field of the concerning electromagnetic wave, respectively. And $\varepsilon_{\text{fluc}}(r)$ is defined as $\varepsilon_{\text{fluc}}(r) = \varepsilon(r) - 1$, where $\varepsilon(r)$ is the relative dielectric constant. Schrödinger equation for electrons with wavefunction $\Psi(\mathbf{r})$ can be written as follows,

$$\left[-\frac{\hbar^2}{2m} \nabla^2 + V(r) \right] \Psi(\mathbf{r}) = E \Psi(\mathbf{r}), \quad (6.2)$$

where m , $V(r)$, and E means the electron mass, the potential energy, and the energy of the electron. The term $-\omega^2/c^2 \varepsilon_{\text{fluc}}(r)$ in equation (6.1) corresponds to $V(r)$ in equation (6.2). John deduced photonic bandgap by applying the free-electron approximation to equation (6.1), and suggested that disturbance in $\varepsilon_{\text{fluc}}(r)$ resulted in localization of electromagnetic waves. Actually, the defect modes appear in the photonic bandgap when a defect is introduced in the photonic crystal. And because such modes in the photonic bandgap cannot exist outside the defect, light can be localized in the defect.

The nanostructures studied here also utilize the above-mentioned specific natures of photonic crystals. Prior to fabricating AlN-based photonic crystals, structural designs were considered especially focusing on technological requirements. Calculations were performed with a commercial software RSoft Photonics CAD Suite, in which plane-wave expansion method was used. At first, slab thickness was determined to be 120 nm, which came from the technological limitation of the MOCVD growth. That means, when the AlN buffer layer was thinner than 100 nm, optical properties of the GaN QDs on it would be deteriorated considerably. Although it has been recently recognized that crystalline quality of the buffer layer can be improved through optimization of

growth conditions and the thickness of the buffer layer can be thinner than 100 nm, the thinnest thickness for the practical buffer layer was considered to be 100 nm at this simulation. Fig. 6.1 shows calculated photonic band edges of the AlN 2-dimensional photonic crystal slab with 120 nm. 2-dimensional triangular lattice photonic crystal pattern with periodicity a and radius of airholes r was considered in the simulation. In the figure, results under three cases were presented simultaneously: $r/a = 0.25, 0.30, 0.32$. From this figure, one can understand that to coincide the photonic bandgap energy with GaN quantum dot luminescence (300 ~ 400 nm), the periodicity of the photonic crystal must be as small as 150 nm or less. Airhole radius must be larger than $0.25a$.

In Figure 6.2, the calculated photonic band diagram of AlN photonic crystal with $a = 150$ nm and $r/a = 0.30$ is shown. There also indicated the light lines of air ($n = 1.0$) and SiC ($n = 2.83$). Because of smaller refractive index of AlN, all photonic bandgap exist above the light line of SiC, which means the photons emitted from GaN quantum dots are able to escape into SiC substrate. In order to obtain sufficient optical confinement in the photonic crystal nanocavities, one must separate the SiC substrate from AlN slab.

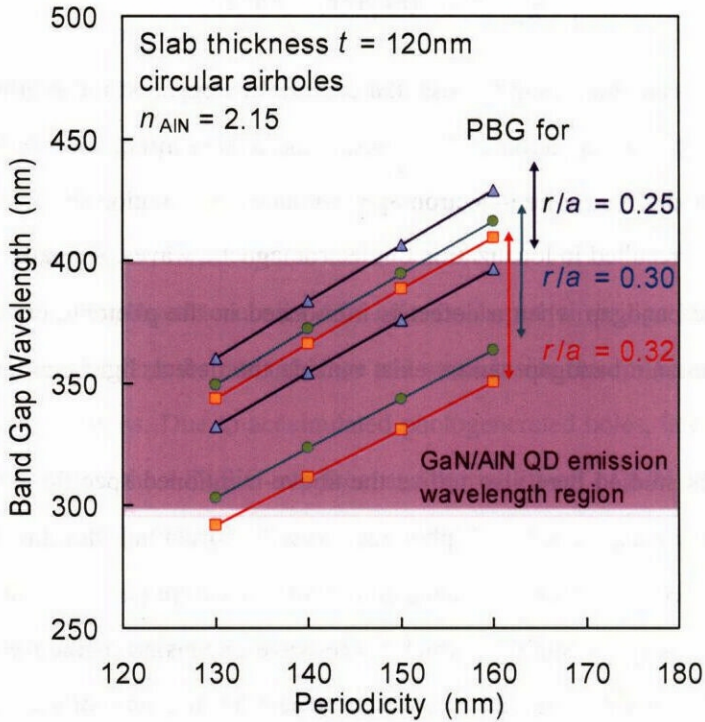


Figure 6.1 Periodicity dependence of photonic band edges of AlN photonic crystal nanocavities

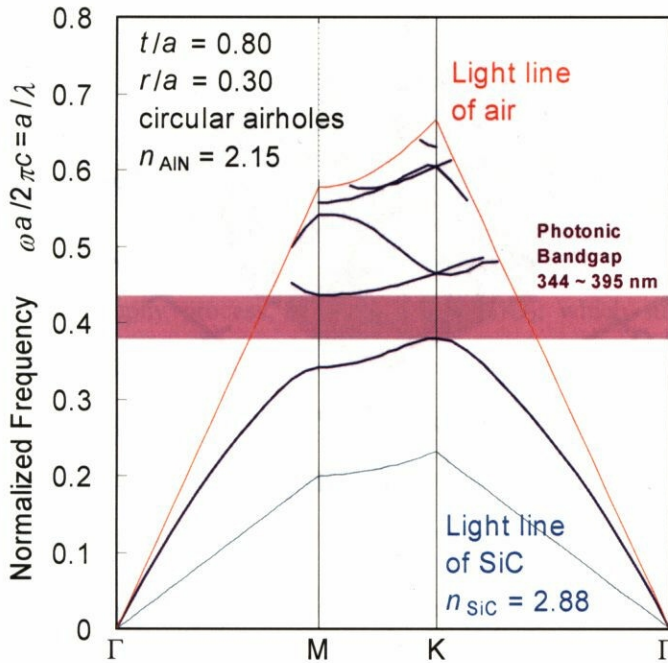


Figure 6.2 A photonic band diagram of AlN photonic crystal nanocavities

6.3 Fabrication process: patterning fine structures

GaN/AlN quantum dot samples were grown by low-pressure metalorganic chemical vapor deposition system, as described in chapter 2. At first, a 100-nm-thick AlN layer was grown on n-type 6H-SiC (0001) substrates at 1180 °C without any buffer layer. Self-assembled GaN quantum dots were then grown in Stranski-Krastanov mode on the AlN at around 960 °C, followed by the two-step growth of an AlN capping layer: firstly a 4-nm-thick layer at the quantum-dot growth temperature and secondly a 16-nm-thick layer at 1180 °C. A reference sample without capping layer was prepared with the same conditions to investigate surface morphology of the GaN quantum dots. Figure 6.3 shows an atomic force microscope image of the reference sample. Density, average height and diameter of the dots were $2.3 \times 10^{10} \text{ cm}^{-2}$, 4.6 nm, and 29 nm, respectively.

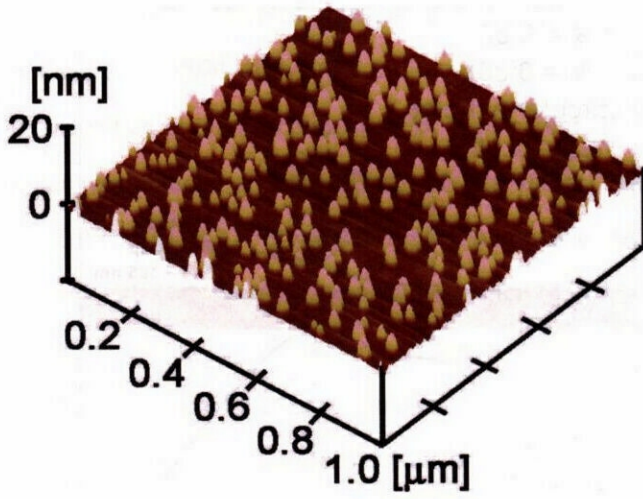


Figure 6.3 An atomic force microscope image of GaN/AlN quantum dots

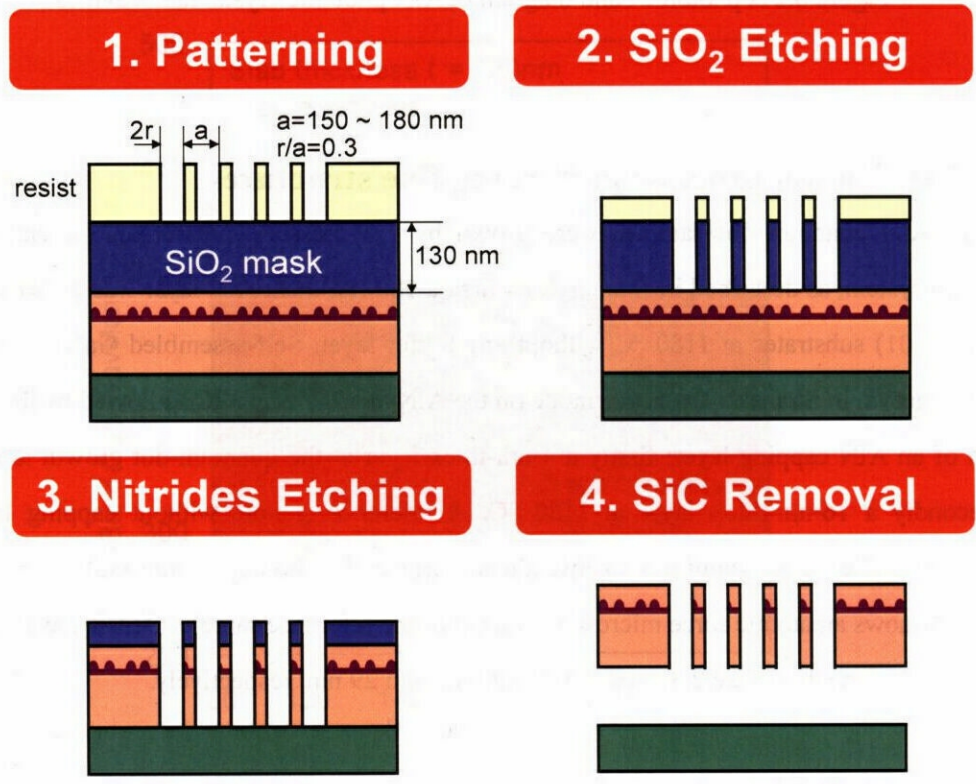


Figure 6.4 Schematic diagram of fabrication processes for AlN photonic crystal nanocavities

Figure 6.4 illustrates schematic diagram of fabrication process used in this study. Triangular lattice photonic crystal patterns with various periodicities (a) and a fixed radius-to-period ratio (r/a) of 0.30 were prepared by electron-beam lithography and inductively-coupled plasma reactive ion etching (ICP-RIE), followed by SiC removal process.

At first, the samples were degreased with acetone followed by methanol. Ultrasonic cleaner was used for the cleaning. Then samples were then rinsed by deionized water, and were dried with N_2 blow. Prior to the lithography process, a 130-nm-thick SiO_2 , which subsequently served as an etching mask for nitride etching, was deposited on the surface by magnetron sputtering. Sputtering conditions were as follows; Ar 12 sccm, O_2 3 sccm, RF power 300 W, and pre-sputtering cleaning time 5 min. Deposition rate of SiO_2 under this conditions was 13 nm/min. Samples were not intentionally heated during the process. Operating pressure was on the order of 1 Pa, while the background pressure was prepared to be below 5×10^{-4} Pa. Thickness of the SiO_2 mask was determined so that one can etch the underlying nitride layers down to the SiC substrate with the mask, preserving designed airhole radius^[133]. Since r/a should be appropriately large enough as mentioned above, care was taken not to shrink the airhole radius especially for such a small a as 150 nm, that may be frequently caused by the etching using a too-thick mask. After the SiO_2 deposition, samples were loaded into an electron-beam evaporator to deposit a Ni (100 nm)/Au (100 nm) contact on backside of the SiC substrate. The contact was used for photoelectrochemical etching of the substrate, which is described in the next section in detail. Surfaces of the SiO_2 -coated samples were carefully treated so as not to contaminate them during the contact evaporation.

Next, an electron-beam resist (Nihon-Zeon, ZEP520A) was spun-coated onto the SiO_2 -coated surface. The conditions for the spin-coating process was as follows; spin-speed/duration (1st step) 500 rpm/ 5 sec, spin-speed/duration (2nd step) 4000 rpm/ 60 sec, and pre-baking 180 °C/ 20 min in an oven. Using these conditions, approximately 300-nm-thick resist layers could be obtained. We prepared the photonic crystal patterns with various periodicities ($a = 120 \sim 200$ nm, 10-nm step) and a fixed radius-to-period ratio (r/a) of 0.30. Each patterns were drawn within a rectangular area of $30a$ (Γ -K direction) $\times 15\sqrt{3}a$ (perpendicular to Γ -K direction), centered on a defect nanocavity. Two sets of the photonic crystal patterns with different defect structure were prepared. One is a defect consists of three missing holes along the Γ -K direction (L3 defect) and the other is a defect with seven missing holes along the Γ -K direction (L7 defect). The photonic crystal patterns were arrayed 70 μm apart from each other. This arrangement allows one to fabricate and characterize the photonic

crystal structures without any interference from neighboring ones ^[133]. Using electron-beam lithography system (JEOL EBX-6000), exposure was performed with following conditions: 50 kV, -120 pA, modulated 20 % (overdose condition) for better reproducibility of the process. For development and rinse, n-amyl acetate (Nihon-Zeon, ZED-N50) and mixed solvent (Nihon-Zeon, ZMD-B) were used at 10 °C, respectively. Development time required was somewhat unstable, probably due to slight perturbations unavoidably introduced during EB-resist preparation. Typically 5 or 6 minutes is appropriate to develop the patterns. Rinse time was 15 sec. We can obtain as small as 140-nm-periodicity patterns with these conditions for EB lithography. Below that, resist collapsed at the narrowest regions between neighboring airholes. It seems reasonable considering that the resist width at the narrowest points in the 130-nm-periodicity pattern is $0.4a = 52$ nm, which is very close to the reported resolution limit of ZEP resist (~ 50 nm).

The photonic crystal patterns were subsequently transferred into underlying SiO₂ by using CF₄/Ar RIE. As shown in the gas-flow diagram (Figure 6.5), we supplied oxygen gas alternatively with duration of several seconds per a minute run of etching to avoid residue to be left inside trenches. By employing this procedure, vertical sidewall of the mask, which is a prerequisite for patterning fine feature in the following steps, can be obtained ^[133]. Flow rates of the process gases used were 5 sccm for CF₄, 2 sccm for Ar, and 2 sccm for O₂, respectively. The ICP power and the bias power were 125 W and 300W, respectively, throughout the process. The pressure during the process was set to be 0.75 Pa. As mentioned earlier, vertical and smooth sidewalls of the trenches are quite important for precise patterning of the nitride layers. Resist can be shrunk by heating during the process, causing tapered etching profiles of the trenches. Relatively high bias power allows one to reduce the shrinkage effects.

Nitride materials were then etched down to the SiC substrate by using Cl₂/Ar RIE. Conditions were as follows: Cl₂ 5 sccm, Ar 1.5 sccm, ICP power 200 W, bias power 500 W, initial pressure 1.2 Pa, final pressure 0.5 Pa, and temperature 50 °C. Typical etching rate of AlN under these conditions was around 120 ~ 150 nm/min. A 1-minute etching usually gave us acceptable results. After the etching, samples were investigated by scanning electron microscope to check the results. Slight faceting of the sidewalls of the airholes was sometimes observed at this stage. This can be attributed to the crystal-orientation dependent chemical reactions, further discussion will be given below.

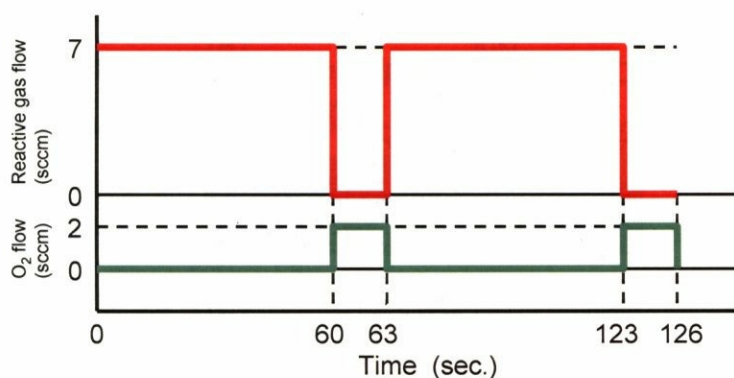


Figure 6.5 Gas flow diagram for SiO₂ etching

6.4 Photoelectrochemical etching of SiC substrate

Since the refractive index of 6H-SiC (2.83) is higher than that of AlN (2.2), the substrate must be removed in order to sufficiently confine optical modes inside the AlN photonic crystal nanocavity. For that purpose, we employed photoelectrochemical wet etching techniques. Our experimental setup, as shown schematically in Fig. 6.6, was similar as that Mikami et al. reported^[134]. The sample was supported by a clamp also served as an electrode and partially dipped in 0.1 % hydrofluoric-acid electrolyte at room temperature. A direct-current bias voltage was applied to the sample via the Ni/Au nonalloyed ohmic contact evaporated on backside of the SiC substrate, while a Pt ribbon was used as a cathode. High-pressure mercury lamp (100 W) was irradiated onto the sample to generate carriers in SiC. Following etching reactions are occurred during the process^[135]:



Overall reaction can be described as follows:



In general, photogenerated carriers play critical roles in photoelectrochemical etching reactions. Therefore we carefully prepared an optical filter not to etch GaN (bandgap energy: 3.39 eV at room temperature) layer itself: wavelength shorter than 370 nm (3.35 eV) was cut off. In the above-mentioned reactions, photogenerated holes (h^+) are the major driving force for resolving SiC into the electrolyte. In the sample, photogenerated holes were predominantly accumulated just below the AlN/SiC interface due to valence band offset (Fig. 6.7, Fig. 6.8a). Due to this accumulation,

etching of SiC proceeded preferentially in lateral direction along the interface under adequate bias conditions (Figs. 6.8b, 6.8c). Typical lateral etching rate of n-type 6H-SiC (0001) with carrier concentration of $\sim 2 \times 10^{18} \text{ cm}^{-3}$ was about 1,000 ~ 1,500 nm/min at a constant bias of + 8.0 V. At this bias, current density of around 0.5 mA/cm^2 was obtained. In this case, vertical etching rate of SiC was much slower ($< 10 \text{ nm/min}$) than lateral direction and anodic oxidation occurred with porous SiC remaining ^[135, 136]. Finally, strain-relieved layer formed convex structure as illustrated in Fig. 6.8d.

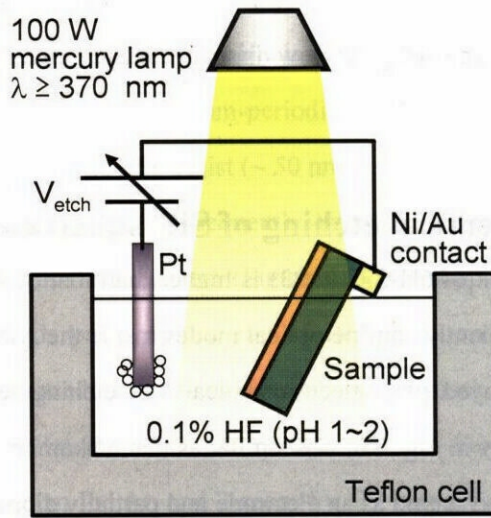


Figure 6.6 Experimental setup of photoelectrochemical etching of SiC

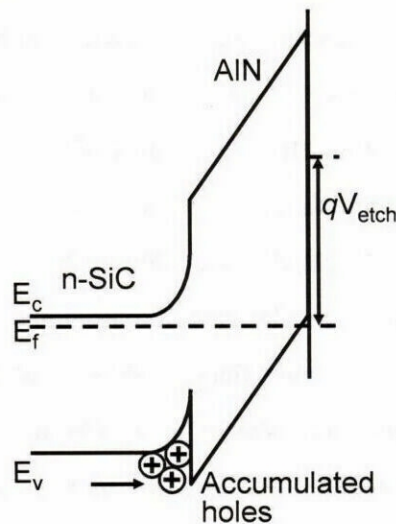


Figure 6.7 Schematic energy band diagram of AlN/SiC interface under a bias

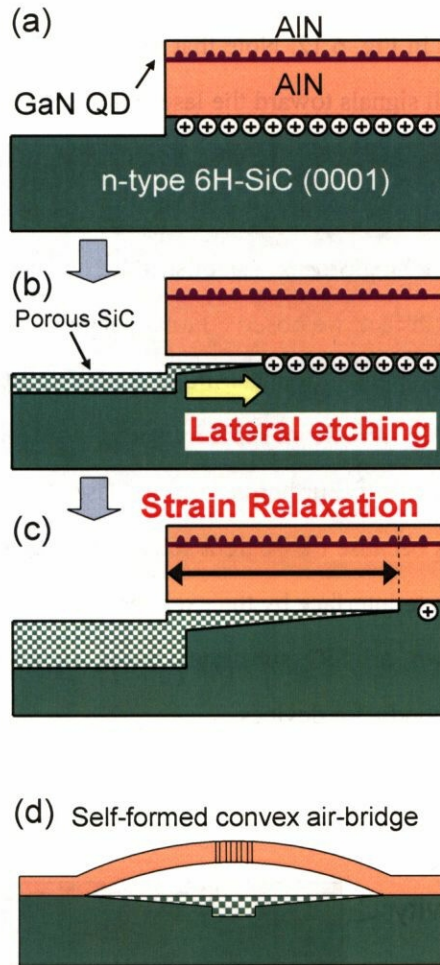


Figure 6.8 Schematic illustration explaining lateral etching of SiC

Schematic illustrations of the fabricated structure are shown in Fig. 6.9. In the upper panel of the figure, a magnified view of the photonic crystal nanocavity is depicted. In Fig. 6.10, cross-sectional scanning electron microscope images of the air-bridge structure is shown. Lift-off epitaxial layer is clearly observed. In the inset of the figure, a magnified view around the air-bridged photonic crystal slab is shown. However, we have not been able to eliminate a possibility of accidental delamination of the film by cleavage at that time. Non-destructive blue-laser microscope was used to confirm the convex shape of the structure, as shown in Fig. 6.11. Almost spherical domes with height of 600 ~ 1,000 nm and base diameter of 30 ~ 50 μm were formed around the photonic crystal patterns ($\sim 4 \times 4 \mu\text{m}^2$). Radius of curvature was estimated to be approximately 300 μm . Bending seems not to affect properties of the photonic crystal patterned in such a small area. Due to gradient of air-gap

height, interference fringes or so-called Newton's rings could be clearly observed in the structure by optical microscopes as shown in Fig. 6.12. Note that in Fig. 6.11, photonic crystal region at the top of the dome reflected too small signals toward the laser microscope to be measured its correct height. We confirmed good yield for the lift-off process by scanning electron microscope observations. Nitride thin film is rigid enough to support the photonic crystal membranes as we fabricated. It should be mentioned that the etching process established here also provides an alternative way to lift off epitaxial III-nitride layers. In fact, we observed total delamination of AlN film from the substrate under extensive etching experiments. Considering that one must prepare an excimer laser and scanning optics to lift off nitride films from sapphire substrates, the process developed in this study is much simpler than the laser liftoff. Furthermore, since laser liftoff is not applicable to the nitride films grown on SiC substrates because transparent substrate is needed to directly decompose nitride materials just above the substrate interface by the excimer laser irradiation, the first successful liftoff applied to the samples grown on SiC substrates poses significant impact on the fabrication technology of III-nitride semiconductor devices.

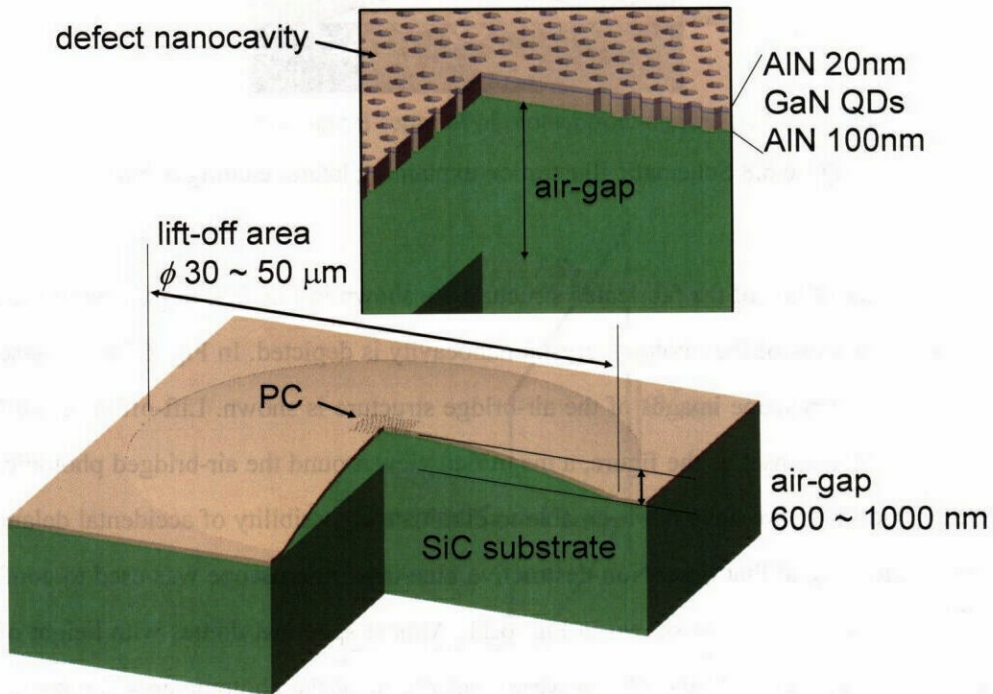


Figure 6.9 Schematic illustration of the fabricated structure

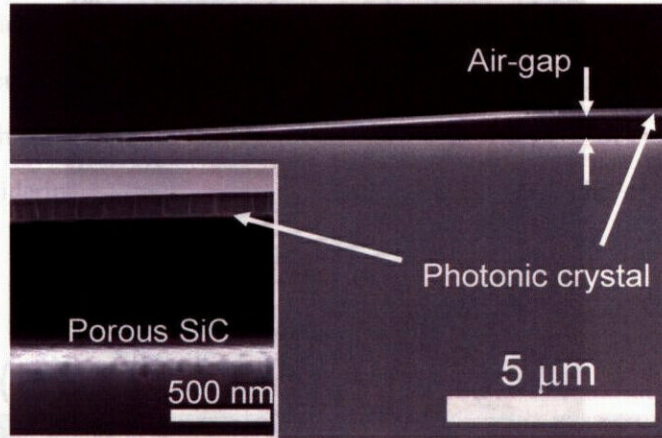


Figure 6.10 Scanning electron microscope images of the air-bridge structure

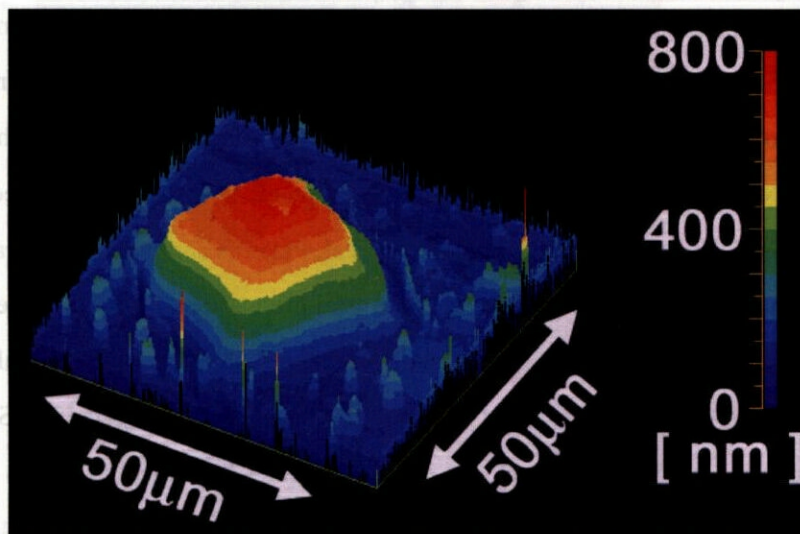


Figure 6.11 A laser microscope image of the fabricated AlN air-bridge structure

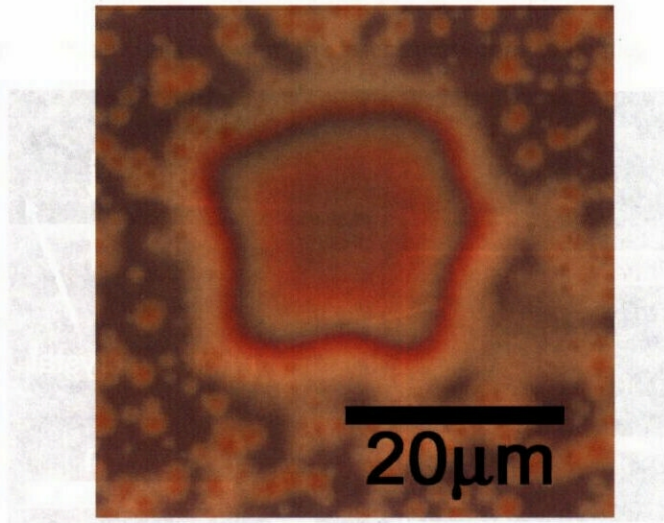


Figure 6.12 Nomarski optical microscope image of the fabricated AlN air-bridge structure

Figures 6.13a, 6.13b, and 6.13c show scanning electron microscope images of a fabricated photonic crystal structure. Photonic crystal patterns with periodicity of as small as 150 nm was successfully fabricated as shown in these images. In spite of using circular shape of mask, hexagonal holes were finally obtained presumably due to crystallographic orientation-dependent chemical reactions during reactive ion etching and photoelectrochemical etching. This phenomenon was not likely attributed to a proximity effect from neighboring holes, since we confirmed that the angle of the hexagon relative to the photonic crystal pattern was dependent on the angle between the a-axis of the epilayer and the Γ -K direction of the photonic crystal. Patterns simultaneously drawn on another sample with various rotation angles relative to the crystal orientation [1-100] were revealed to have hexagonal holes with corresponding rotation angles relative to the photonic crystal pattern. Final surfaces of the sidewall always consisted of family of m-plane {10-10} (Fig. 6.13b). Similar findings on crystallographic orientation-dependent reactivity of GaN in the cases of Cl-based inductively-coupled plasma etching^[137] and KOH wet etching^[138] have been reported. It has been suggested that the largest absolute photonic band gap can be achieved in the case of airholes of the same symmetry as the lattice symmetry^[139]. Naturally-formed hexagonal shape of the airholes will be useful to experimentally investigate the effects of the reduced symmetry in two-dimensional

photonic crystals ^[139, 140]. Smooth and vertical sidewalls were obtained as shown in Fig. 6.13c. Since structural disorders such as surface roughness of the sidewalls may deteriorate quality of the photonic crystals ^[141, 142], these features are highly preferable. As-etched surfaces after the Cl₂-based RIE may have numerous defects due to high-energy ion bombardments. Dry-etched III-nitride crystals usually suffer from the process-induced damages ^[143]. On the contrary, wet chemical etching is regarded as a much softer process. Therefore, the incidental reshaping of the dry-etched airholes is also beneficial considering the most severely damaged portions of the crystals can be removed through the process.

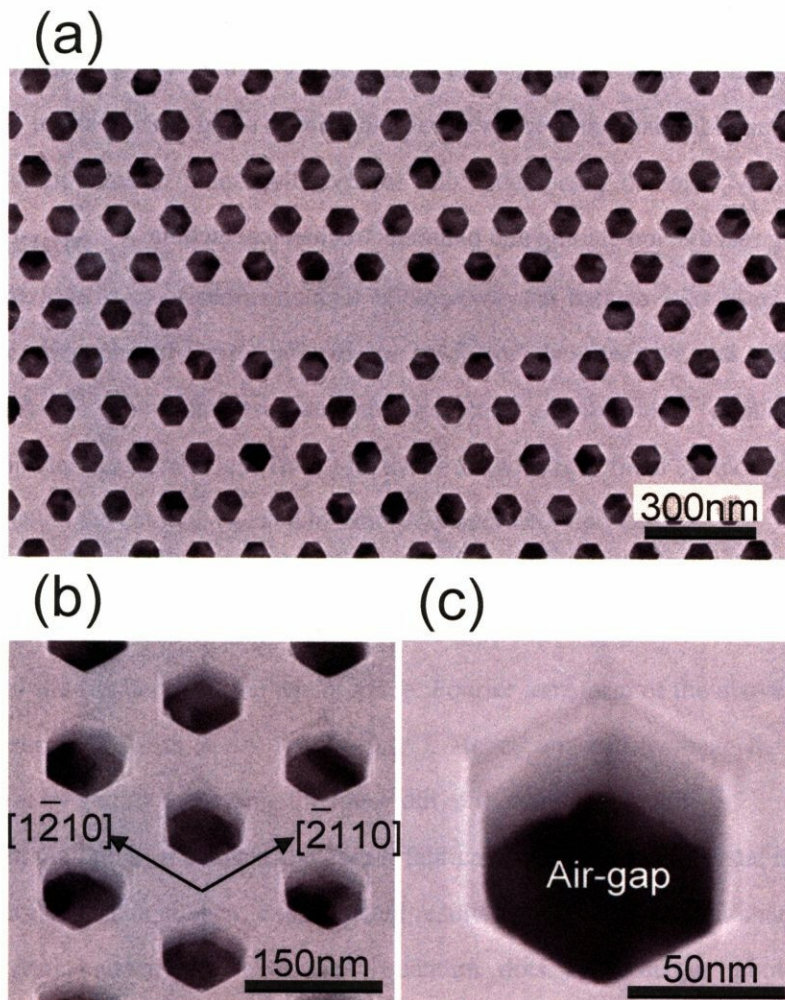


Figure 6.13 SEM images of the fabricated photonic crystal

6.5 Summary

In this chapter, the fabrication processes developed for air-bridge AlN photonic crystal nanocavities was described in detail. Corresponding to the short-wavelength of GaN quantum dot emission, fine patterns as small as 150-nm-period is required. Also, the 6H-SiC substrate must be removed in order to obtain sufficient optical confinement in the nanocavities. To this end, the author developed efficient way to remove SiC substrate with photoelectrochemical etching. And he could fabricate AlN air-bridge photonic crystal nanocavity by using this technique for the first time. Energy band discontinuity at epitaxial layer/substrate interface and strain inside the epitaxial layer were utilized in the novel fabrication process. The author found that lateral etching of 6H-SiC substrate occurred just below the AlN/SiC interface due to accumulated photogenerated holes, and that partially lifted-off AlN epitaxial layer subsequently formed convex air-bridge structures by relaxation of internal in-plane compressive strain. In spite of using circular shape of mask, hexagonal holes were finally obtained presumably due to crystallographic orientation-dependent chemical reactions during reactive ion etching and photoelectrochemical etching.